Comparative summary of approaches used with the impulse response method

Comparative summary of approaches used with the impulse response method

M. Wermbter[1], L. Altenbach[1], O. Detlefsen[1] and M. Abdel-Maksoud[1]

[1] Institute for Fluid Dynamics and Ship Theory, Hamburg University of Technology (TUHH), Am Schwarzenberg-Campus 4, 21073 Hamburg, Germany

E-mail: malwin.wermbter@tuhh.de

Abstract. This paper presents a comparison of various methodologies to calculate the seakeeping behaviour of ships using the impulse response method. Developments of several authors incorporate non-linearities regarding the radiation, diffraction and wave forces. In contrast to frequency domain methods, advantages are expected if ship motions become non-linear, for example in waves with high steepness ratios. The comparison is structured into analysis for each force component with and without motions in waves. The main contribution is the quantitative analysis for several ships, forward speeds and methodologies. Multiple frequency domain methods are incorporated in the analysis. The focus of the analysis lies on the evaluation of applicability as well as the limits of the method for all states investigated. The results of the impulse response method show the following: The method is applicable to several forward speeds. In long waves, the choice of the parameters calculated in the frequency domain for the computation of the radiation and diffraction forces has a strong influence on the computed motion amplitudes. In short waves, the computation of the added resistance is a considerable challenge. Especially at high forward speeds, the consideration of the stationary wave system is essential for obtaining accurate results with three-dimensional panel codes.

1. Introduction

Motion simulations in seaways are categorised by their level of non-linearity and the required effort of calculation. The impulse response method is a time-domain approach, which allows to incorporate non-linearities in each force component, however the simulations are faster than real-time. Existing publications present a variety of approaches to simulate the ship motion in regular and irregular waves, as well as special topics as green water on deck [1], hydroelastic calculations [35], parametric rolling [18] or dynamic positioning [6]. Although, it is unclear which approach has the most advantages in terms of efficiency and accuracy. In order to categorise various seakeeping methods, Hirdaris [13] developed a six level system. The current state-of-the-art impulse response methods are to be assigned to level 2, Froude-Krylov non-linear methods. Some authors [24, 26] have incorporated body-non-linearity into radiation forces to reach level 3. Other differences between existing publications relate to the coordinate system used for the motion integration and force calculation, the method used for frequency domain coefficients and the calculation of Froude-Krylov, restoring, radiation and diffraction forces.

1.1. Coordinate system

Ship motions are usually described in three coordinate systems. A global, hydrodynamic and ship-fixed system [11]. Newtons 2nd Law is used to calculate the ship motions either in the inertial hydrodynamic or global coordinate system or in the non-inertial ship-fixed coordinate system. If the motions are calculated in the non-inertial frame additional Coriolis forces due to the acceleration of the coordinate system have to be considered. Approaches by Fossen [11], Kristiansen [17], Perez [22], Hirdaris [14],Ballard [3] apply this principle. The reason to use this coordinate frame is either the formulation of the frequency domain coefficients or the application of control forces, which are usually formulated in the ship-fixed frame. Perez [21] compared the developed formulations in both coordinate system, when using the strip theory with and without forward speed. Most publications use the hydrodynamic coordinate system to calculate the ship motion. The publications by Riesner [28, 26, 27, 25] are especially relevant for this paper, since the applied three-dimensional panel code is the same as in this publication. The main advantage of the formulation in the inertial coordinate system is that the Coriolis forces are not required and the frequency domain coefficients can be directly used.

1.2. Frequency domain coefficients

The radiation and diffraction forces in the impulse response method are calculated by using coefficients from frequency domain programs. Frequency domain codes are classified into Green and Rankine type sources and strip or three-dimensional discretisations. Strip theory is mostly based on the formulations by Salvesen [31] or Bertram [4], it is assumed that the change in flow quantities along the ship's length is small and negligible. Three dimensional calculations require higher computational effort, however the stationary wave system and the change in flow quantities along the ship length can be calculated. Green-function methods require only the discretisation of the hull, whereas Rankine-source methods require the discretisation of the hull and the free surface [8, 34]. In principle all methodologies can account for forward speed, however strip theory calculations are only corrected by considering the longitudinal change of the main sectional area, which neglects the influence of the stationary wave system. The coefficients for the hydrodynamic added mass, the hydrodynamic damping are solved by calculating the forces on a moving ship in still water, the so-called radiation problem to determine the added mass and damping. The diffraction coefficients are determined by measuring the forces on a fixed ship and subtracting the Froude-Krylov and restoring forces [8]. The coefficients for the Froude-Krylov and restoring forces may also be used in the impulse-response method, however the computational power has increased to a level, where these forces can be calculated in every time step on a panel grid. When transforming the radiation forces from frequency domain to time domain using the formulation by Cummins [5], the resulting force amplitude and phase in the time-domain is not equal to the frequency domain coefficients. Therefore, Fonseca [10] and Ma [19] introduced the so-called radiation restoring matrix using two different formulations. Riesner [27] developed a radiation restoring coefficient for the three-dimensional panel code used in their calculations.

1.3. Wave and restoring force calculations with panel grids

Froude-Krylov and restoring forces are calculated using panel grids and evaluating the Bernoulli pressure on every panel in each time step. The reason for this methodology is that these forces are dominant and non-linear, if the wave amplitudes are high or the body geometry exhibits large local changes. Hirdaris [14] highlighted the force imbalance which arises from the non-linear and linear mixture of force components. In order to prevent an ever increasing drift motion, soft springs are usually applied to hold the ship in a time-averaged position. The panel grid used in the calculations is usually composed of triangular or quadrilateral panels. Differences in the force calculation arise for the stretching scheme, the order of integration

and at the waterline, where panel cutting or panel deformation schemes are used. Stretching schemes are introduced due to the fact, that the Bernoulli pressure is only valid up to the still waterline. Above it, the pressure exponent e^{-kz} is positive and pressures increase exponentially. Although, the pressure at the free-surface is clearly defined as air pressure. In order to correct the inaccuracies of the Airy-wave theory, stretching schemes are introduced which force the pressure to be equal to the air pressure at the free surface. A popular and easy applicable stretching scheme is the so-called Wheeler-Stretching [36]. Alternatively, linear extrapolation is sometimes used, however only accurate for wave amplitudes which are significantly much smaller than the ship dimensions [35]. Du [7] compared mapping methods, Wheeler-Stretching in linear and non-linear waves and showed that the mapping methods are closest to the wave pressures by 5th order Stokes theory, but due to the simplicity of Wheeler-Stretching and acceptable accuracy, this method seems to be the most efficient solution. Riesner [28] deformed the mesh to the current waterline and applied Wheeler stretching for every panel to accurately capture the pressure above the still waterline. The pressure is assumed to be constant above the panel area. Rodrigues [29] developed an adaptive mesh refinement with quadrilateral panels and exact integrations of the Bernoulli pressure by using Green's theorem for integrals. Zhang [37] used the same approach, however formulated the forces directly in the ship-fixed coordinate system. Exact integrations of the Bernoulli pressure is favourable at locations where the panel size is big relative to the pressure gradients. Theoretically, the panels can be made infinitely big, if the geometry is accurately represented, as the computational effort decreases only if the number of panels is reduced. Although, the formulations for Froude-Krylov forces are more accurate than constant pressure calculations, the additional effort for hydrostatic forces is not required, since the hydrostatic pressure is linear and the force always equal to the submergence depth of the center of area multiplied with the area. In relation to the integration of Froude-Krylov pressures, this paper follows a new approach and integrates the pressure exactly along the area of triangular panels, without the need of coordinate transformations.

1.4. Radiation forces

Radiation forces in the impulse response method incorporate the memory effect of ship motions. The memory effect describes the time-dependency of forces and ship motions due to the radiating waves. The calculation of the forces is done with the convolution integral or state-space models. Convolution integrals require higher computational effort than state-space methods. However, the identification of state-space models is challenging and various methods for identifying the parameters exist, see for example Kristiansen [17], Perez [22], Hatecke [12], Roessling [30], Peña-Sanchez [23]. In order to reduce the simulation time, a limited order of states is used, theoretically the state-space formulation is equal to the convolution integral when using infinite states. Input to both formulations is either the hydrodynamic damping or added mass, most publications use the hydrodynamic damping, because the boundary values are clearly defined. Perez [20] discussed the limits of the retardation functions, which are integrated from the frequency domain damping. The proposed boundary value extrapolation is used in many publications and efficiently avoids oscillations in the retardation functions. Recent publications did not further incorporate state-space models, since the simulation time depends mainly on the pressure calculations with panel grids. Although recent developments were made by incorporating body non-linearity into the radiation forces. Rajendran [24] calculated radiation forces for several draughts and for each strip individually. In the time-domain, the convolution integral is reformulated for every time step and saved until the retardation function has decayed. This has a considerable influence on the bending moments and the added resistance. Riesner [26] assumed linear pressure distributions above the still waterline to the current waterline and developed a formulation for the panel radiation pressures, without the need for a new convolution formulation. The influence on the added resistance is significant.

1.5. Diffraction forces

Diffraction forces arise due to the reflection of waves at the ship. It is assumed that the response is linear to the incoming wave in the frequency domain codes. In the time-domain these coefficients are multiplied with the wave elevation at the midship section [6]. Some authors also include impulse response functions for diffraction forces [3, 14, 15, 37]. Differences are only visible if the wave elevation at the midship section becomes non-linear. This effect is only present, if the ship motions or rotations are non-linear, since the Airy-wave theory is always linear.

1.6. Paper structure

The contribution of this paper can be summarised as a comparison of forces for several formulations, extracting knowledge about the formulations and limitations and areas of application. The paper may help other researches and software developers to choose the approach suitable for the field of application. Chapter 2 gives a brief overview of the force calculations as well as the motion integrations. Chapter 3 introduces the simulation parameters and the investigated ship geometries. A post-Panamax container ship DTC [9] and the Kriso container ship [16] are investigated. Chapter 4 shows the results for each force component for fixed DTC and the response amplitude operators (RAO) as well as the added resistance for the DTC and KCS at several forward speeds. In the last chapter 5 the findings are summarised and concluded. The appendix lists additional formulae for the exact pressure integration.

2. Methodologies

2.1. Coordinate systems

Ship motions are described by three coordinate systems. A global coordinate system is fixed to the still water plane with the z-axis pointing downwards. The x and y-axis are orientated arbitrarily, usually in the ship longitudinal and transversal axis. The hydrodynamic coordinate system is also fixed to the still water plane, but moves with the average ship forward speed. The x-axis points in the direction of the time-averaged longitudinal ship axis and y to starboard. The origin of the hydrodynamic system is chosen to be at the main frame, midship and at the still water level. Ship motions are described by the ship moving relative to the hydrodynamic coordinate system, therefore a ship-fixed coordinate system is introduced, which is fixed to the main frame, midship and the initial draft. The ship-fixed coordinate system is participating in all rotations.

The coordinates of a coordinate vector in global coordinates $\vec{\xi_g}$ follow from the hydrodynamic coordinates by adding the longitudinal translation from the average ship speed $\vec{U} = [u, 0, 0]^T$ and the constant yaw angle $\bar{\psi}$

$$\vec{\xi_g} = \vec{U} \cdot t + \boldsymbol{R}_{\mathrm{z},\bar{\psi}} \vec{\xi} \,. \tag{1}$$

The transformation matrix $\boldsymbol{R}_{\mathrm{z},\bar{\psi}}$ describes a rotation around the vertical z-axis.

A ship-fixed point $\vec{\xi}_{\mathrm{P}}$ in hydrodynamic coordinates is calculated with the Euler angle transformations $\boldsymbol{R}^h_{\mathrm{b}}$ of the ship-fixed position vector $\vec{x}_{\mathrm{P}}$ and the vector of the coordinate origin $\vec{\xi}$ expressed in hydrodynamic coordinates

$$\vec{\xi}_{\mathrm{P}} = \vec{\xi} + \boldsymbol{R}^h_{\mathrm{b}} \cdot \vec{x}_{\mathrm{P}} \,. \tag{2}$$

The transformation matrix is composed from the yaw-pitch-roll transformation matrices

$$\boldsymbol{R}^h_{\mathrm{b}} = \boldsymbol{R}_{\mathrm{z},\psi} \cdot \boldsymbol{R}_{\mathrm{y},\theta} \cdot \boldsymbol{R}_{\mathrm{x},\phi} \,, \tag{3}$$

$$= \begin{bmatrix} \cos\psi & -\sin\psi & 0 \\ \sin\psi & \cos\psi & 0 \\ 0 & 0 & 1 \end{bmatrix} \cdot \begin{bmatrix} \cos\theta & 0 & \sin\theta \\ 0 & 1 & 0 \\ -\sin\theta & 0 & \cos\theta \end{bmatrix} \cdot \begin{bmatrix} 1 & 0 & 0 \\ 0 & \cos\phi & -\sin\phi \\ 0 & \sin\phi & \cos\phi \end{bmatrix} . \tag{4}$$

The angular velocities $\vec{\omega}$ obtained from the equation of motions are transformed to Euler angle derivatives by

$$\dot{\vec{\Theta}} = \boldsymbol{T}\vec{\omega} = \begin{bmatrix} 1 & \sin\phi\tan\theta & \cos\phi\tan\theta \\ 0 & \cos\phi & sin\phi \\ 0 & \frac{\sin\phi}{\cos\theta} & \frac{\cos\phi}{\cos\theta} \end{bmatrix} \cdot \vec{\omega}\,, \tag{5}$$

the initial value problem is updated every time step.

2.2. Equation of motion

According to Cummins [5] the equation of motion using impulse response functions includes the hydrodynamic mass matrix at infinite frequency $\boldsymbol{A}(\infty)$, the hydrodynamic damping at infinite frequency $\boldsymbol{B}(\infty)$, the retardation function matrix $\boldsymbol{K}(t)$ and external forces

$$(\boldsymbol{M} + \boldsymbol{A}_\infty)\ddot{\vec{\xi}} + \boldsymbol{B}_\infty\dot{\vec{\xi}} + \int_0^t \boldsymbol{K}(t)\dot{\vec{\xi}}(t-\tau)d\tau + C_\mathrm{R}\vec{\xi} = \vec{F}_\mathrm{D} + \vec{F}_\mathrm{FK+R} + \vec{F}_\mathrm{S} + \vec{F}_\mathrm{ext}\,. \tag{6}$$

The formulation in (6) differs from the original formulation. The restoring matrix $\boldsymbol{C}$ is replaced with non linear restoring and exciting wave forces $\vec{F}_\mathrm{FK+R}$. Additionally, the radiation restoring matrix $\boldsymbol{C}_\mathrm{R}$ is added, which is derived by for example Fonseca [10] and arises due to the differences between the time domain and frequency domain equation. The calculation of these forces and moments, as well as the calculation of the diffraction force $\vec{F}_\mathrm{D}$ and the soft mooring force $\vec{F}_\mathrm{S}$ is explained in the following sections. The vector $\vec{F}_\mathrm{ext}$ may include arbitrary external forces, but is neglected in this paper.

If the Cummins equation is formulated in body-fixed coordinates, additional Coriolis forces arise due to the rotation of the body-fixed frame around the inertial axis of the hydrodynamic coordinate system [11]. An advantage of this formulation is the direct integration of arbitrary ship-fixed forces and a constant right-hand side, which leads to more stable accelerations and allows to use bigger time steps

$$(\boldsymbol{M} + \boldsymbol{A}_\infty)\ddot{\vec{x}} + \boldsymbol{B}_\infty\dot{\vec{x}} + \int_0^t \boldsymbol{K}(t)\delta\dot{\vec{x}}(t-\tau)d\tau + C_\mathrm{R}\vec{x} = \vec{F}_\mathrm{D} + \vec{F}_\mathrm{FK+R} + \vec{F}_\mathrm{S} + \vec{F}_\mathrm{ext} - m\cdot\boldsymbol{L}\dot{\vec{x}}\,. \tag{7}$$

Where $\dot{\vec{x}}$ is the velocity vector expressed in ship-fixed coordinates relative to the global coordinate system. $\delta\vec{x}$ is the the velocity expressed in ship-fixed coordinate relative to the hydrodynamic coordinate system, which is obtained by subtracting the constant velocity vector

$$\delta\dot{\vec{x}} = \dot{\vec{x}} - \boldsymbol{R}^T\vec{U}\,. \tag{8}$$

The Coriolis forces in vectorial form are described by the matrix $\boldsymbol{L}$, which simplifies $m\vec{\omega}\times\dot{\vec{x}}$

$$\boldsymbol{L} = \begin{pmatrix} 0 & 0 & 0 & 0 & 0 & 0 \\ 0 & 0 & 0 & 0 & 0 & 1 \\ 0 & 0 & 0 & 0 & -1 & 0 \\ 0 & 0 & 0 & 0 & 0 & 0 \\ 0 & 0 & 0 & 0 & 0 & 0 \\ 0 & 0 & 0 & 0 & 0 & 0 \end{pmatrix}. \tag{9}$$

Frequency domain coefficients are determined with the strip theory *PDStrip* and the three-dimensional panel code *panFDS*, which requires the stationary wave system from *GLRankine*. The theory of the programs is extensively described in [8].

2.3. Diffraction forces

Forces arising due to reflection of waves at structures are described as diffraction forces. Their calculation in the impulse response method is based on the coefficients obtained from the frequency domain calculations. Two methods are present in the literature. In one method the frequency domain coefficients are transformed into the time domain by multiplying with the wave elevation at the coordinate origin

$$\vec{F}_{\mathrm{D,linear}}(t) = \Re(\vec{\hat{D}}_{\mu_\mathrm{e},\mathrm{T}}(\omega_\mathrm{e})\hat{\zeta}e^{i(\omega t - kx\cos\mu + ky\sin\mu + \varphi)}) \tag{10}$$

Where $\vec{\hat{D}}_{\mathrm{r},\mu_\mathrm{e},\mathrm{T}}$ is the complex diffraction force coefficient for the current encounter angle μ_e and the current draught T. The wave elevation with the amplitude $\hat{\zeta}$ and the phase φ is evaluated at the position $x(t), y(t)$ of the coordinate origin.

The second method is introduced by Bailey [2] and calculates a diffraction impulse response function $\vec{K}_\mathrm{D}$. Hirdaris [14] arguments that the wave elevation at the midship can become non-linear

$$\vec{K}_\mathrm{D}(t) = \frac{1}{\pi}\int_0^\infty \vec{D}_\mathrm{r}(\omega_\mathrm{e})\cos(\omega_\mathrm{e}\tau) - \vec{D}_\mathrm{i}(\omega_\mathrm{e})\sin(\omega_\mathrm{e}\tau)\ \mathrm{d}\omega_\mathrm{e}\,. \tag{11}$$

Where the diffraction force coefficient is split into its real part $\vec{D}_\mathrm{r}$ and imaginary part $\vec{D}_\mathrm{i}$. The diffraction force is calculated with a convolution integral

$$\vec{F}_{\mathrm{D,conv}} = \int_0^t \vec{K}_{\mathrm{D},\mu_\mathrm{e},\mathrm{T}}(\tau)\zeta(t-\tau)\ \mathrm{d}\tau\,. \tag{12}$$

$\zeta(t)$ is the real part of the wave elevation in (10). The memory consumption of this formulation is significantly higher than the formulation in (10), since all wave elevations of the last n time steps have to be saved, until the diffraction retardation function is fully decayed. The decay time is for the investigated ships around 15-30 seconds. If the body-non-linearity is used, the last n draughts have to be saved additionally to select and interpolate the retardation functions to each draught.

The implementation of the diffraction retardation function is automated with the use of splines. The retardation functions are integrated and afterwards fitted with a C-Spline. The usage of splines allows to evaluate the retardation functions at every time instant. Different draughts than the initial draughts of the frequency domain calculations are interpolated. This requires sufficiently close arranged draughts.

2.4. Froude-Krylov and restoring forces

Froude-Krylov and restoring forces arise from the wave pressures and the submergence of the ship body. The pressure is described by the Bernoulli equation

$$p_{\mathrm{FK+R}} = \rho g z - \rho\dot{\phi} - \rho g\zeta_\mathrm{st}\,. \tag{13}$$

With the submergence depth z and the free surface height due to the stationary wave system ζ_st. The stationary wave is interpreted as an additional contribution to the hydrostatic pressure. The assumption applied is that the stationary wave system is not changing relative to the ship and the velocities are small. Froude-Krylov forces arise due to the time derivative of the wave potential $\dot{\phi}$ which is described by

$$\dot{\phi}(x,y,z,t) = \hat{\zeta}ge^{-k(z-\zeta)}\cos(\omega t - kx\cos\mu + ky\sin\mu + \varphi)\,. \tag{14}$$

Where the exponent in the classical formulation e^{-kz} [8] is modified to $e^{-k(z-\zeta)}$. This technique is called Wheeler stretching [36], because the pressure for coordinates with $z < 0$ is exponentially growing. The resulting pressure at the free surface is only valid for small wave amplitudes and the stretching forces it to be equal to the atmospheric pressure. The technique is widely used and has been investigated for example by Du [7].

In natural seaways, the pressure is formulated for every wave component individually and summed afterwards. However, the wave elevation in the pressure always refers to the sum of all wave components for every component.

The resulting force and moment vector on the ship can be calculated from the pressure by multiplying it with the normal vector $\vec{n}$ and integrating it over the ship surface

$$\vec{F} = \int_S p_{\mathrm{FK+R}} \vec{n} \, \mathrm{d}S \,, \tag{15}$$

$$\vec{M} = \int_S p_{\mathrm{FK+R}} (\vec{x}_{\mathrm{P}} - \vec{x}_{\mathrm{G}}) \times \vec{n} \, \mathrm{d}S \,. \tag{16}$$

The moment vector is additionally multiplied with the distance of a point $\vec{x}_{\mathrm{P}}$ to the position of the center of gravity x_{G}.

In order to evaluate the pressure on the ship, the ship is meshed with n_{P} triangular panels. Each panel is seen as individual object and the forces of each panel are summed to the total force

$$\vec{F} = \sum_{\mathrm{i}=1}^{n_{\mathrm{P}}} \int_S p_{\mathrm{FK+R,i}} \vec{n}_i \, \mathrm{d}S_{\mathrm{P}} \,, \tag{17}$$

$$\vec{M} = \sum_{\mathrm{i}=1}^{n_{\mathrm{P}}} \int_S p_{\mathrm{FK+R,i}} (x_{\mathrm{P,i}} - x_{\mathrm{G}}) \times \vec{n}_i \, \mathrm{d}S_{\mathrm{P}} \,. \tag{18}$$

The pressure on a panel can be integrated analytically or can be taken as constant and multiplied with the panel area A

$$\vec{F} = \sum_{\mathrm{i}=1}^{n_{\mathrm{P}}} p_{\mathrm{FK+R,i}} \vec{n}_i A_i \,. \tag{19}$$

The point of pressure evaluation $\vec{x}_{\mathrm{P}}$ is taken as the center of the submerged panel area

$$\vec{x}_{\mathrm{P}} = \sum_{\mathrm{i}=1}^{3} \frac{\vec{x}_i}{3} \,. \tag{20}$$

This assumption leads to exact hydrostatic forces, since the hydrostatic pressure is linear and the area above and below the center of area is always equal to the integral of the pressure.

The direct integration by Rodrigues [29] or Zhang [37] is done by using Green's theorem. The following formulae are derived by direct integration of the wave pressures over the panel area. The integration allows to use significantly larger panels for the evaluation of the Froude-Krylov forces. As long as the panel size is not reducing the shape accuracy, the panels can be theoretically infinitely large.

The total force on a panel is the sum of the integrated force for two triangles

$$F_{\mathrm{fk}} = F_{\mathrm{fk,1}} + F_{\mathrm{fk,2}} \,. \tag{21}$$

An example panel is shown in Figure 1. For the integration of the area, the each panel is split into two separate triangular areas. If the panel intersects the free surface, it is additionally split

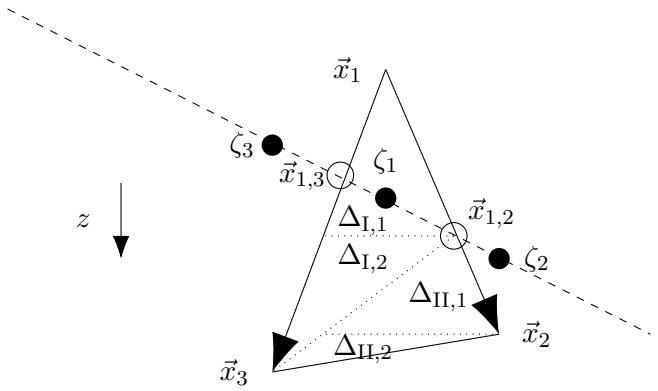

Figure 1: Schematic view of a panel intersecting the free surface

into additional triangles I and II, indicated by the dotted line from $\vec{x}_{1,2}$ to $\vec{x}_3$. The separate panels corner points are sorted by their z-coordinate amplitude. The integration is done for the upper and lower panels separately, the horizontal line from $\vec{x}_{1,2}$ and $\vec{x}_2$ show the triangles.

The derivation of the formulations is shown in the appendix. For non-horizontal panels, inserting the equations (48) into the force at a specific height (52) leads to the forces

$$F_{\mathrm{fk},1} = a_1 \Bigg[\frac{e^{-kz_1} \cdot (k \sin\beta \sin(c_2 L_1 + b_1) + c_2 \cos(c_2 L_1 + b_1)) - e^{-kz_0} (k \sin\beta \sin(b_1) + c_2 \cos(b_1))}{k^2 \sin^2\beta + c_2^2} \tag{22}$$

$$+ \frac{e^{-kz_1} \cdot (-k \sin\beta \sin(b_2 L_1 + b_1) - b_2 \cos(b_2 L_1 + b_1)) - e^{-kz_0} (-k \sin\beta \sin(b_1) - b_2 \cos(b_1))}{k^2 \sin^2\beta + b_2^2} \Bigg], \tag{23}$$

$$F_{\mathrm{fk},2} = -a_2 \Bigg[\frac{e^{-kz_1} \cdot (k \sin\beta \sin(c_4 L_2 + b_3) + c_4 \cos(c_4 L_2 + b_3)) - e^{-kz_2} (k \sin\beta \sin(b_3) + c_4 \cos(b_3))}{k^2 \sin^2\beta + c_4^2} \tag{24}$$

$$+ \frac{e^{-kz_1} \cdot (-k \sin\beta \sin(b_4 L_2 + b_3) - b_4 \cos(b_4 L_2 + b_3)) - e^{-kz_2} (-k \sin\beta \sin(b_3) - b_4 \cos(b_3))}{k^2 \sin^2\beta + b_4^2} \Bigg], \tag{25}$$

$F_{\mathrm{fk},1}$ is the force for the upper panel and $F_{\mathrm{fk},2}$ for the lower part. The abbreviations are all shown in the appendix.

If a panel is purely horizontal, meaning that $|n_z| = 1$, the sorting of coordinates and the integration is done along the y-direction leading to

$$F_{\mathrm{fk},1} = \begin{cases} a_3 (f_{\mathrm{fk},11} + f_{\mathrm{fk},12}) & y_1 - y_0 \neq 0 \\ 0 & y_1 - y_0 = 0 \end{cases} \tag{26}$$

$$F_{\mathrm{fk},2} = \begin{cases} a_3 (f_{\mathrm{fk},21} + f_{\mathrm{fk},22}) & y_2 - y_1 \neq 0 \\ 0 & y_2 - y_1 = 0 \end{cases} \tag{27}$$

$$\tag{28}$$

Theoretically, the wave elevation ζ, which appears in the Wheeler stretching, is also a function of the panel length and should be integrated too. However, the resulting formulae include a term $e^{\cos(x)} \cdot \cos(x)$, which is not integratable without series approximations and seems not to be a justifiable effort. Therefore, the amplitude in the Wheeler stretching is assumed as constant over the panel length and is evaluated at the panel center of area.

The center of pressure can be integrated by multiplying the pressure with the position vector $\vec{x}$ and integrating the resulting force per area. This work is ongoing and not yet ready to be published. The moments in this paper are calculated relative to the center of the area.

Emerged and partly submerged are identified by their position relative to the free surface at the corner points. Emerged panels are characterised by the fact that all corner point z-coordinates are lower than the wave elevations at their positions. In Figure 1 a partly submerged panel is shown. The free surface is indicated by the dotted line and the intersections of the panel with the free surface as $\vec{x}_{1,3}$ and $\vec{x}_{1,2}$. The intersection is calculated by

$$\vec{x}_{1,\mathrm{i}} = \vec{x}_1 + \frac{z_1 - \zeta_1}{(\zeta_\mathrm{i} - \zeta_1) - (z_\mathrm{i} - z_1)} \cdot (\vec{x}_\mathrm{i} - \vec{x}_1)\,. \tag{29}$$

In order to integrate the resulting quadrilateral, the area is split into two triangular panels $\vec{x}_{1,3}, \vec{x}_{1,2}, \vec{x}_3$ and $\vec{x}_3, \vec{x}_{1,2}, \vec{x}_2$. If only one corner point is submerged, the triangle is formed by the submerged point and the two intersection points.

2.5. Radiation forces

Radiation forces originate from the ship moving in the waves. They are separated into the acceleration dependent hydrodynamic mass $\boldsymbol{A}$, the radiation restoring matrix $\boldsymbol{C}_\mathrm{R}$ and the velocity dependent convolution integral

$$\vec{F}_\mathrm{rad} = -\boldsymbol{C}_\mathrm{R}\vec{x} - \boldsymbol{A}(\infty)\ddot{\vec{x}} - \boldsymbol{B}(\infty)\dot{\vec{x}} - \int_0^t \boldsymbol{K}(t-\tau)\delta\dot{\vec{x}}(\tau)\,\mathrm{d}\tau \tag{30}$$

$$\boldsymbol{K}(t) = \frac{2}{\pi}\int_0^\infty (\boldsymbol{B}(\omega) - \boldsymbol{B}(\infty))\cos(\omega t)\,\mathrm{d}\omega \tag{31}$$

Perez [20] established formulas for the asymptotic behaviour of the diagonal entries of the hydrodynamic damping $\boldsymbol{B}$. The resulting retardation function $\boldsymbol{K}(t)$ is sensitive to high frequent oscillations, if the damping at high frequencies is not zero. In case of the formulation in (31), the difference at low frequencies should not be lower than zero, leading to an excitation of the motion. The proposed boundary values for the retardation function can also be integrated analytically as done by Riesner [28]. In this publication, the boundary values have been approximated with the formulation by Perez [20], the integration afterwards is done numerically. Since the boundary values at infinity are zero, the radiation forces are integrated without subtracting the damping.

Fonseca [10], Riesner [27], Ma [19] introduced various formulations for radiation restoring coefficients. The resulting forces are required, since the formulation of the Cummins equation is not equal to the frequency domain equation of motion. The formulation by Fonseca [10] and Ma [19] refer to strip theory coefficients. The formulation by Fonseca is used in this paper due to its simplicity of implementation

$$\boldsymbol{C}_\mathrm{R,2d} = \omega_\mathrm{e}^2\,(\boldsymbol{A}(\infty) - \boldsymbol{A}(\omega_\mathrm{e})) - \omega_\mathrm{e}\int_0^\infty \boldsymbol{K}(\tau)\sin(\omega_\mathrm{e}\tau)\,\mathrm{d}\tau\,. \tag{32}$$

For the three-dimensional panel code, Riesner [28] subdivided the panel pressure into frequency dependent and frequency independent parts, which leads to the restoring coefficient matrix, when these pressures are integrated over all panels for each radiation problem

$$\boldsymbol{C}_\mathrm{R,3d} = \int_A -\left(\vec{U} + \nabla\phi^0\right)(\vec{\alpha}\times\nabla\phi^0)\,. \tag{33}$$

In order to introduce non-linearities into the radiation forces, the convolution integral and the hydrodynamic mass is calculated for several draughts and interpolated in every time step during the simulation

$$\vec{F}_\mathrm{rad} = -\boldsymbol{C}_\mathrm{R}(z)\vec{x} - \boldsymbol{A}(\infty, z)\ddot{\vec{x}} - \int_0^t \boldsymbol{K}(t-\tau, z)\dot{\vec{x}}(\tau)d\tau \tag{34}$$

$$\approx -\boldsymbol{C}_\mathrm{R}(z_n)\vec{x} - \boldsymbol{A}(\infty, z_n)\ddot{\vec{x}}(t_\mathrm{n}) - \frac{\mathrm{dt}}{2}\cdot\left(\boldsymbol{K}(t_n, z_n)\dot{\vec{x}}(t_0) + 2\sum_{\mathrm{i}=1}^{n-1}\boldsymbol{K}(t_{\mathrm{n-i}}, z_{\mathrm{n-i}})\dot{\vec{x}}(t_i) + \boldsymbol{K}(t_0, z_0)\dot{\vec{x}}(t_n)\right). \tag{35}$$

The computational effort for the evaluation of the integral is increased because the retardation functions for a specific draught z_i have to be saved until the function is decayed.

2.6. Soft mooring force

Imbalances due to the different level of non-linearities in the force components and the missing propulsion force can lead to constantly increasing surge, sway and yaw motions [14]. These motions are non-physical and can be prevented by a spring force and moment. The spring forces are calculated based on the position of the ship in the hydrodynamic coordinate frame and are assumed to act in the hydrodynamic coordinate axis. The force is composed of a linear spring force with constant c_s and a damping force linear to the velocities with the damping constant d_s

$$\vec{F}_\mathrm{sm} = -\begin{pmatrix} \xi \\ \eta \\ 0 \\ 0 \\ 0 \\ \psi L_\mathrm{PP} \end{pmatrix} c_\mathrm{s} - \begin{pmatrix} \dot{\xi} \\ \dot{\eta} \\ 0 \\ 0 \\ 0 \\ \dot{\psi} L_\mathrm{PP} \end{pmatrix} d_\mathrm{s} \,. \tag{36}$$

The constants are chosen based on the heave eigenfrequency. One sixth of the eigenfrequency is used to calculate the spring constant and the damping constant to ensure that the soft mooring is not influencing the heave, roll or pitch motion

$$c_\mathrm{s} = \frac{\Delta\omega_3^2}{36} \,, \qquad d_\mathrm{s} = \frac{\Delta\omega_3}{6} \,. \tag{37}$$

3. Ship geometries and simulation parameters

The panel grid on the hulls of the Duisburg Test Case (DTC) and the Kriso Container Ship (KCS) are shown in Figure 2a and Figure 2b. The main particulars are listed in Table 1. The investigated speeds orientate at the existing model test data and RANS simulations, which are $Fn = 0.139$ for the DTC and $Fn = 0.26, 0.33, 0.4$ for the KCS.

The DTC is a post-Panamax container ship with a full-scale length of 355 m with a capacity of 14000 TEU [9]. The KCS is smaller with a length of 230 m [33]. Both ships are extensively validated and investigated and validated in the literature.

Table 1: Main particulars of DTC and KCS in model size

	DTC	KCS
λ	59.4	38.59
L_{PP}[m]	5.976	5,96
B_{wl} [m]	0.859	0.83
T_m [m]	0.244	0.279
∇ [m^3]	0.827	0.976
COG_x [m]	2.907	3.06
COG_y [m]	0.0	0,0
COG_z [m]	0.4	0.381
r_{xx} [m]	0.4B	0.4B
r_{yy} [m]	0.25L	0.25L
r_{zz} [m]	0.25L	0.25L

Table 2: Wave length and height combinations for simulations with fixed DTC

λ/L_PP	$H[m]$
2.5	0.2
1.8	0.2
1.4	0.2
1.2	0.138
1.09	0.15
1.0	0.158
0.91	0.128
0.8	0.134
0.6	0.1

In the following section, a comparison of the force amplitudes for the DTC in regular waves is presented. These amplitudes are compared with results obtained by Riesner [25] and use the wave length and wave heights shown in Table 2.

(a) DTC (b) KCS

Figure 2: Panel grids used in the time and frequency domain simulation

4. Results

The following section contains results for the fixed DTC container ship, as well as results for the freely moving DTC and KCS. The comparison for the fixed ship is verified with CFD results presented by Riesner [25]. The response amplitude operators for heave and pitch are compared with experimental results by Sigmund [32] (DTC) and Simonsen [33] (KCS). The response amplitude operator for heave is normalised with the wave amplitude ζ

$$Y_3 = \frac{z}{\zeta}\,, \tag{38}$$

and the pitch motion is made non-dimensional with the wave steepness

$$Y_5 = \frac{\theta}{k\zeta}\,. \tag{39}$$

The added resistance in waves is normalised with the ship length and breadth

$$C_{\mathrm{AW}} = \frac{F_{\mathrm{x,avg}} L_{\mathrm{PP}}}{\rho g B^2 \zeta^2}\,. \tag{40}$$

The evaluation of the added resistance is challenging, since the amplitude is small compared to the harmonic amplitudes. The force average of all external forces is subtracted by the average of the longitudinal hydrostatic pressure. This is required, since the stern of the ships is not wetted and therefore not covered with panels. The resulting hydrostatic force in combination with the pressures due to the stationary resistance are not part of the added resistance. It is important, that the equilibrium state of the ship is equal to the desired floating condition, otherwise the added resistance in short waves may become inaccurate.

4.1. Forces on fixed DTC container ship

In Figure 3, the energy of the force calculated from its Fourier transform is compared for different number of panels. The amplitudes are normalised with the amplitude obtained at the highest number of panels, which is assumed to be most accurate. The simulation is done with a wavelength of $\lambda/L_{\mathrm{PP}} = 2.5$ and a steepness of $H/\lambda = 0.01$. The hydrostatic and Froude-Krylov forces are separately calculated and compared for the exact pressure integrations and the constant pressure evaluations.

The differences in between force amplitudes from coarse to fine panel discretisations is greater for the hydrostatic forces. Hydrostatic forces are equal for every discretisation, if the geometry is represented accurately. Therefore, the differences arise due to the inaccurate representation of the surface of the ship with low panel numbers. The difference between exact and constant hydrostatic pressures arises due to the applied splitting scheme. The results for exact panels are subdivided at the waterline, whereas the constant panel calculations approximate the hydrostatic pressure at the waterline by calculating the new center of the submerged area. It is assumed, that the surface is linear between its intersections. This simplification leads to difficulties at the transom stern, which emerges during the simulation and the panels intersecting the free surface may experience highly non-linear intersecting curves.

The Froude-Krylov forces show smaller dependency on the discretisation, the exact pressure integrations are less sensible to the number of panels. The additional effort of integrating the pressure may be beneficial if the grid is refined manually after the generation with *GLRankine*. At the current state, the form accuracy limits the benefit of exact integrations. A typical number of panels for frequency domain calculations is around 2000 panels per ship. This level of discretisation seems to be accurate enough for the time domain simulation and is used in every following simulation.

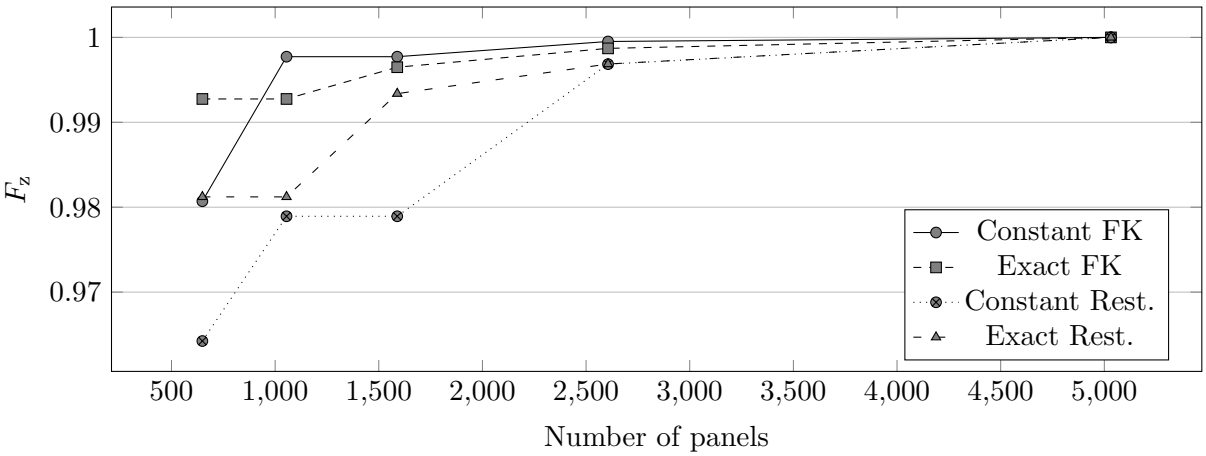

Figure 3: Comparative grid study for hydrostatic and Froude-Krylov forces with exact pressure integrations and constant pressure evaluations in a regular wave of length $\lambda/L_{\mathrm{PP}} = 2.5$ and a steepness of $H/\lambda = 0.01$

Figure 4 shows the absolute value of the diffraction force coefficient for heave motion. The frequency coefficients from the strip theory *PDStrip* and the panel code *panFDS* are compared with the force amplitudes from a time domain simulation (TD coefficient/TD convolution) with the coefficient and convolution approach.

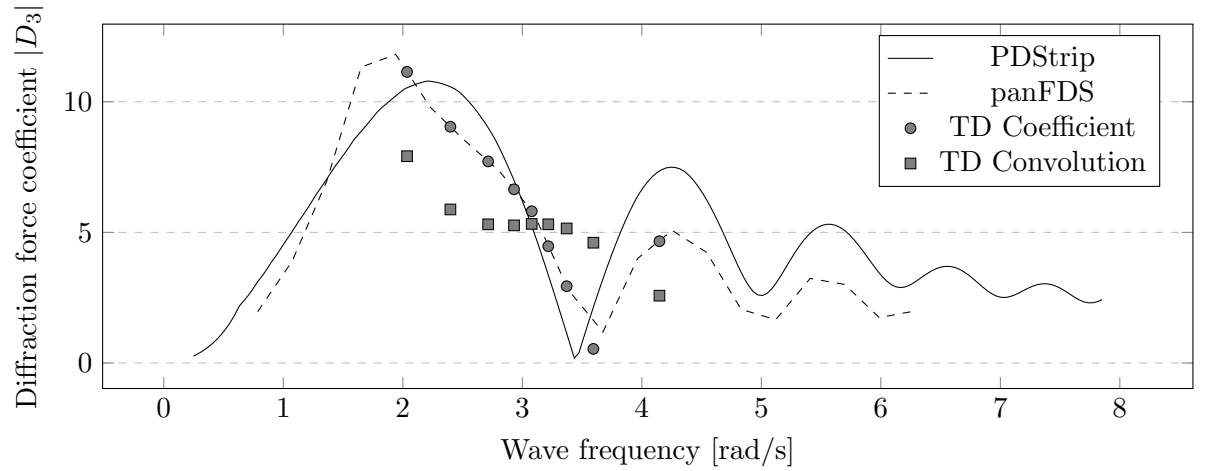

Figure 4: Normalised diffraction force $|D_3| = |F_3/\zeta|$ amplitudes in time and frequency domain

It is visible, that the transformation into time domain and retransformation into frequency domain does not lead to differences between the *panFDS* results and the *TD Coefficient* results. The *PDStrip* coefficients show slightly increased higher order amplitudes, but a lower first order amplitude. The convolution diffraction function significantly affects the force amplitudes. The peaks from the linear calculations are no longer present and the amplitudes are slowly decaying with increasing wave frequency.

In Figure 5 the radiation force amplitudes are compared for a calculation with constant retardation functions and a constant hydrodynamic mass matrix as well as the interpolation approach presented in subsection 2.5. The radiation restoring coefficient is yet neglected.

The comparison of force amplitudes shows that the first order peaks are not influenced by the calculation method, however the second order peak is significantly larger for the variable calculation. The FFT of the force signal calculated with variable radiation forces shows even higher orders of forces,

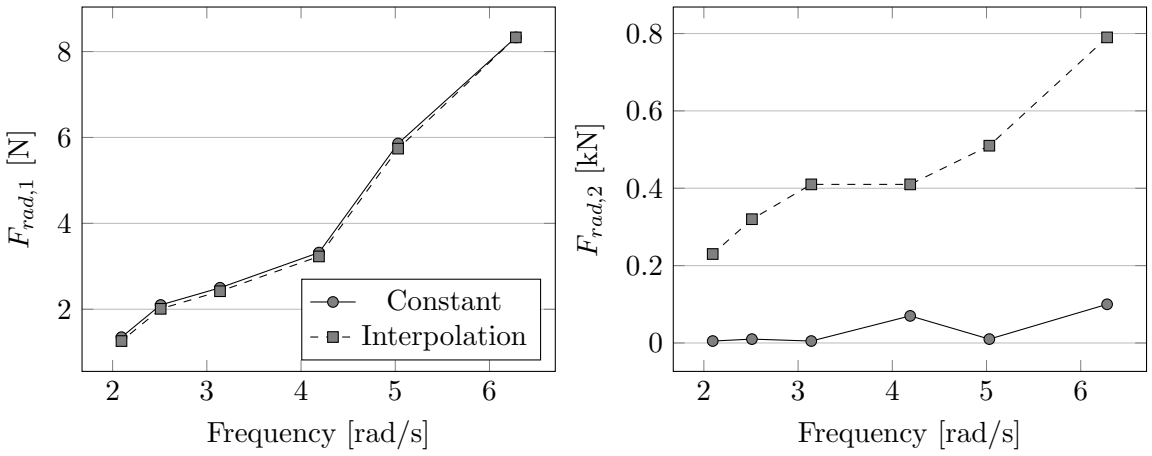

Figure 5: Comparison of vertical radiation force amplitudes for 1st and 2nd order motion frequency due to forced heave motion of the DTC with amplitude of 0.12 m

however their amplitude is negligible small. The amplitudes of the constant calculation show only one peak at the motion frequency and decay afterwards. The higher order force is explainable with the variation of the hydrodynamic mass and the retardation. If it is assumed that the hydrodynamic mass varies linearly with the draught, the force is described by the product of two harmonic functions

$$\boldsymbol{A}(z,t) = (\boldsymbol{A}(\infty) + \boldsymbol{\delta A}(\infty) sin(\omega t))\zeta \sin(\omega t)\,, \tag{41}$$

where the added mass variation $\boldsymbol{\delta A}(\infty)(t)$ oscillates with twice the frequency as the motion frequency ω.

The following figures Figure 6-Figure 8 show comparisons of force calculations with CFD results by Riesner [25]. The DTC container ship is fixed in head waves with wave heights and wavelength according to Table 2. The left figures show the first order force and moment amplitudes and the right figures the second order force and moment amplitudes. Results for the third and fourth order amplitude are also available, but not presented due to negligible amplitudes.

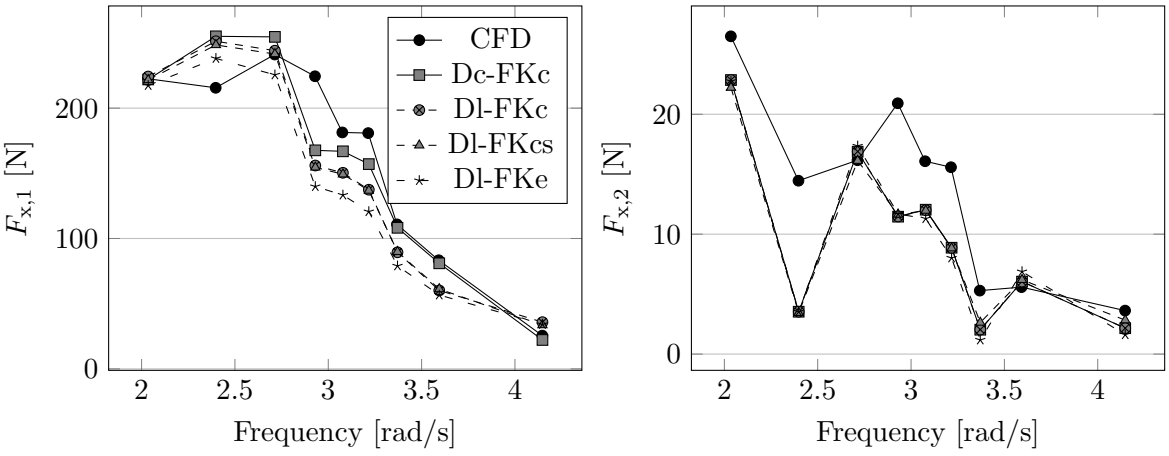

Figure 6: DTC force amplitudes in longitudinal direction of first and second order in head waves with $Fn = 0.139$ for various diffraction (D) and Froude-Krylov (FK) calculations. The diffraction parameters are convolution (Dc), linear (Dl) and the Froude-Krylov parameters stand for constant (FKc), exact (FKe) and constant with stationary surface (FKcs).

Figure 6 shows the longitudinal forces on the DTC ship in head waves at a forward speed corresponding to a Froude number of $Fn = 0.139$. Over all simulation settings the forces are in range of the CFD

calculations. The difference for first order forces is large in the range around 3 $\frac{\text{rad}}{\text{s}}$ and is almost equal at the lowest and highest simulated wave frequency. The value of the second order force is around 10% of the first order amplitudes and the impulse response simulations do not differ from each other, however the differences to the CFD results are higher in percentage. The diffraction calculation with a convolution integral (Dc-FKc) leads to higher first order longitudinal forces. The consideration of stationary pressures in the Froude-Krylov calculation (Dl-FKcs) does not influence the calculation of longitudinal forces and results in approximately the same force amplitude as the linear diffraction and Froude-Krylov calculation (Dl-FKc). The exact integration of the panel pressures (Dl-FKe) leads to lower forces across the whole frequency range. In long waves this reduction leads to a better agreement with the CFD results, whereas in shorter waves, the forces are under predicted.

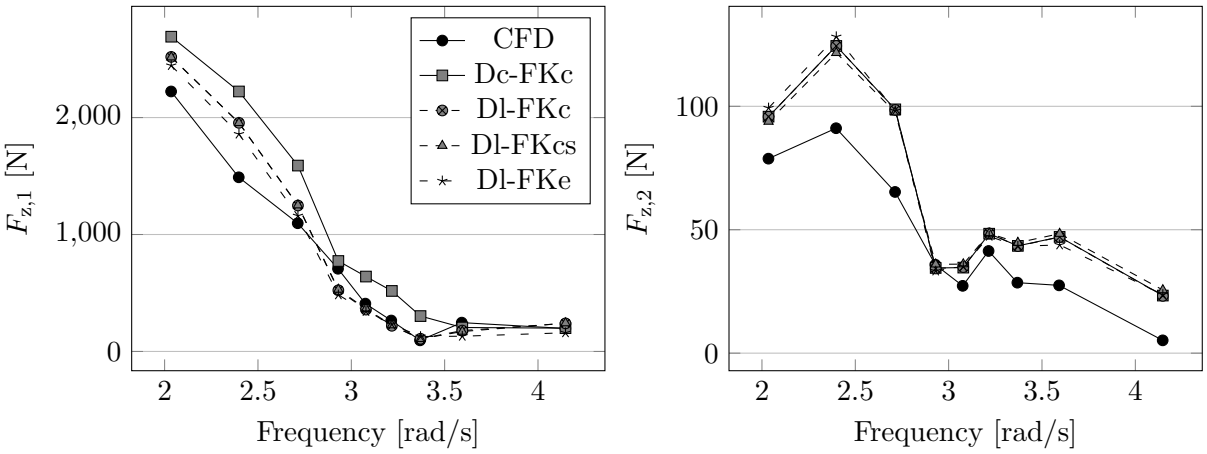

Figure 7: DTC force amplitudes in vertical direction of first and second order in head waves with $Fn = 0.139$ for various diffraction (D) and Froude-Krylov (FK) calculations.

Figure 7 shows the vertical force amplitudes at first and second order of the wave frequency. In comparison to Figure 6 the amplitudes are around 10 times larger and decrease from 2 kN in waves equal to three times the ship length to almost negligible amplitudes in waves shorter than half of the ship length. The second order amplitudes are around 5% of the first order amplitudes. The agreement is better in short waves, whereas in long waves the impulse response method calculations show higher forces than the CFD results. The individual force calculations show a similar trend as for the longitudinal forces, where the diffraction convolution (Dc-FKc) produces higher force amplitudes and the exact pressure integrations (Dl-FKe) lead to smaller force amplitudes than the calculations Dl-FKc and Dl-FKcs, which are closest to the CFD results.

In Figure 8 the pitch moment amplitudes are compared. The calculated values differ in long waves, which is most likely due to the non-linear diffraction forces included in the CFD computations. The reflection of waves is expected to increase at the bow and stern if they are submerged in the wave, which is not covered by the linear frequency domain coefficients. The exact integration leads to significantly higher second order moments, which may originate from the approximation of the point of action at the center of the panels. The determination of the exact point of action is in progress and assumed to reduce the second order force amplitudes.

4.2. Motions and added resistance of DTC in regular waves

The following section shows comparisons of response amplitude operators (RAO) for heave and pitch and the added resistance in head waves at Froude number $Fn = 0.139$. The results are compared with experimental results by Sigmund [32]. The heave and pitch RAO are shown in Figure 9.

The heave motion at the eigenfrequency, indicated by the local peak at 5 $\frac{\text{rad}}{\text{s}}$, is underestimated for the impulse response calculations, except the calculation with convolution diffraction. The diffraction is generally overpredicting the motion amplitudes in heave and pitch. The exact integration of pressures

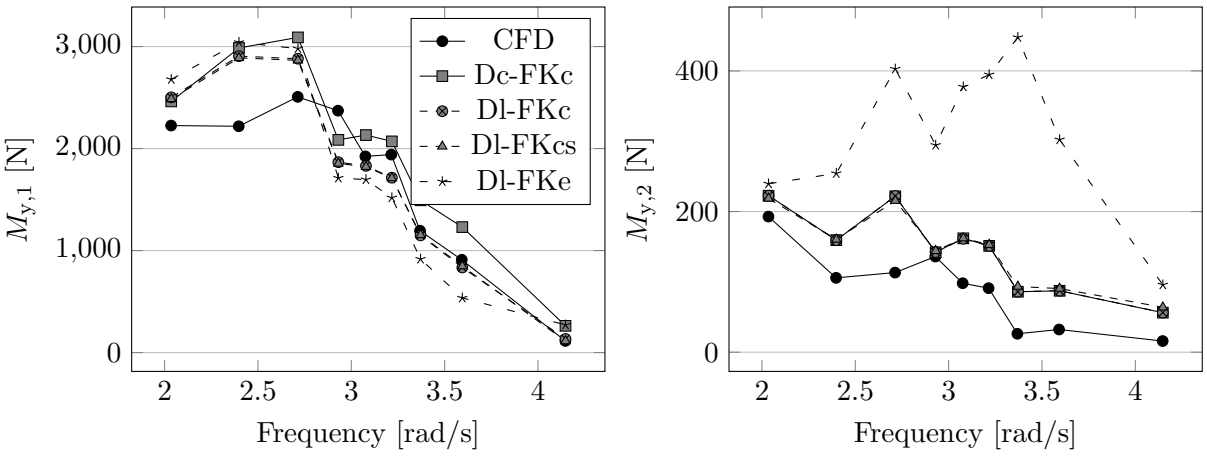

Figure 8: DTC pitch moment amplitudes of first and second order in head waves with $Fn = 0.139$ for various diffraction (D) and Froude-Krylov (FK) calculations.

leads to lower motion amplitudes. The under prediction of the heave and pitch motion may be explained by simplifications related to potential theory, since the frequency domain transfer functions are not representing the peak either.

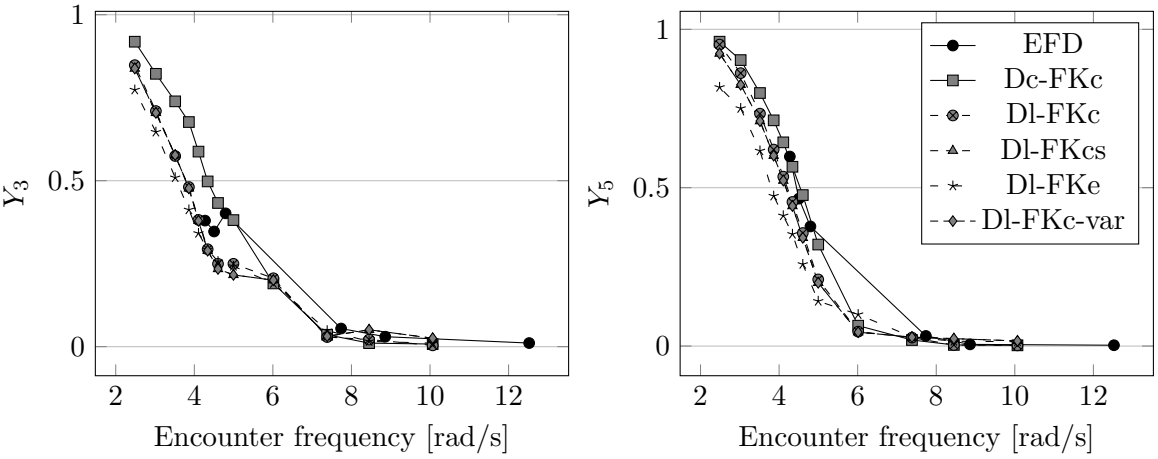

Figure 9: DTC heave (left) and pitch (right) transfer function for $Fn = 0.139$ in head waves

Figure 10 shows the added resistance coefficient C_{AW} plotted over the encounter frequency. The experimental results are taken from Sigmund [32]. The coefficient increases up to the region of the heave and pitch eigenfrequency at approximately 5 $\frac{\mathrm{rad}}{\mathrm{s}}$ and decreases to a constant value at high frequencies, which represents the reflection of incoming waves at the bow. The linear diffraction calculation methods show neglectable differences across the frequency range and a slightly underpredicted peak value, whereas the diffraction convolution method overestimates the peak of the added resistance. The exact integration leads to a slightly negative coefficient at the highest wave frequency. The values at the higher frequencies are highly sensitive to the equilibrium hydrostatic forces. Since the transom is not covered with panels, the longitudinal force is always unequal to zero. If the center of gravity is not exactly above the center of buoyancy, the hydrostatic force will differ at the end of the simulation and cause an error in the calculation of the added resistance.

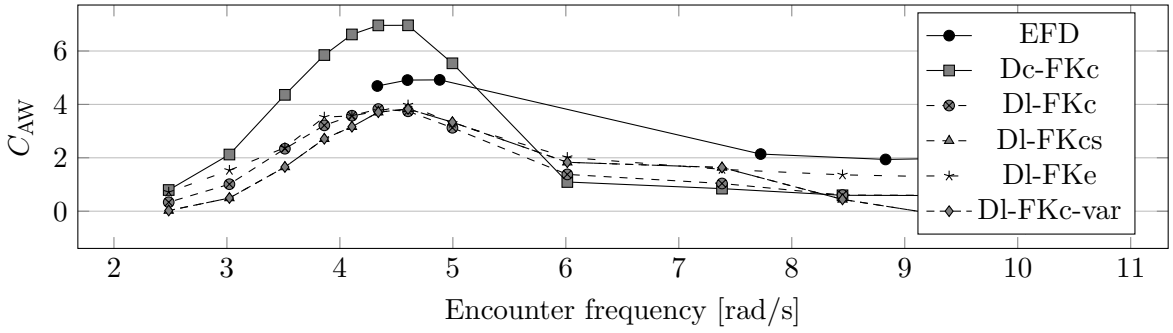

Figure 10: DTC added resistance for $Fn = 0.139$ in head waves

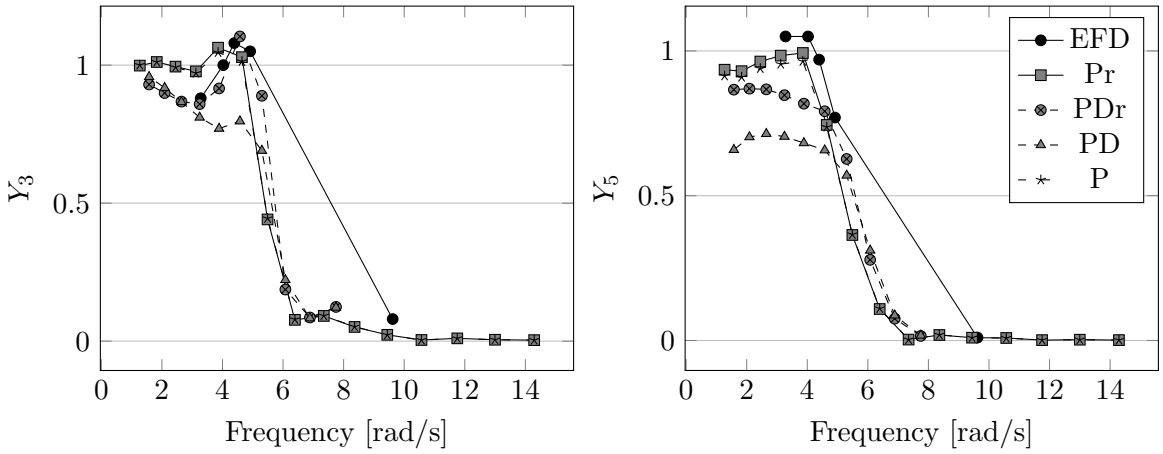

Figure 11: KCS heave (left) and pitch (right) transfer function for $Fn = 0.26$ in head waves

4.3. Motions and added resistance of KCS in regular waves

The simulations for the DTC include a comparison between the force calculation methods. This section contains a comparison for the KCS and the usage of the radiation restoring coefficients as well as strip theory and the three-dimensional panel code *panFDS*. The results are compared against the experimental results by Simonsen [33]. The diffraction force calculation is conducted using the frequency domain coefficients and the panel pressures are calculated with constant pressures along the panel.

Figure 11-Figure 13 show the heave and pitch transfer functions in head waves with a Froude-Number of $Fn = 0.26$, $Fn = 0.33$, $Fn = 0.4$. Different parameter sets are indicated by

- Pr = *panFDS* coefficients and restoring matrix
- P = *panFDS* coefficients
- PDr = *PDStrip* coefficients and restoring matrix
- PD = *PDStrip* coefficients
- EFD = Experimental results by Simonsen [33]

Figure 11 shows the heave and pitch transfer function for $Fn = 0.26$. The heave motion is accurately captured by the simulations, except the strip theory calculations without restoring coefficient. Significant differences are visible for the strip theory coefficient calculations in long waves. Both motions are underestimated, the application of the restoring coefficient leads to an increase in amplitude. As shown by Ma [19], this is a problem when using strip theory coefficients in impulse response formulations with the radiation restoring coefficient by Fonseca [10]. The radiation restoring coefficient by Riesner [25]

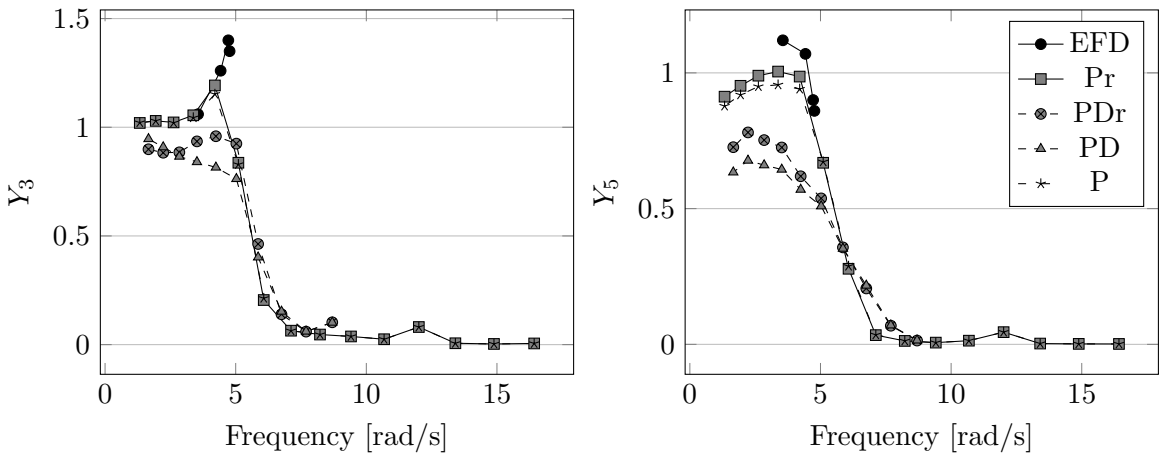

Figure 12: KCS heave (left) and pitch (right) transfer function for $Fn = 0.33$ in head waves

leads to an improvement of the pitch motion amplitudes and should be applied in this speed range, when *panFDS* coefficients are used.

For $Fn = 0.33$ the heave and pitch transfer functions are plotted in Figure 12. The heave and pitch motion are underestimated by the impulse response calculations for the resonance area at approximately $5\,\frac{\text{rad}}{\text{s}}$. The resulting motions are not as close to the experimental results, as the results for the DTC and KCS at lower Froude numbers. The influence of the coupling between the heave and pitch motions is increasing with higher forward speed. The non-diagonal entries of the damping matrix take non-zero values at infinite frequency and the consideration of the boundary values suggested by Perez [20] is no longer straightforward. It is possible to adapt the integration of the retardation functions by subtracting the highest calculated value of the damping, however this often leads to negative damping at low-frequencies which violates the passive system properties [12] and leads to an excitation of the ship motions. The chosen solution procedure presented in subsection 2.5 leads to the most reasonable results for all investigated ship types and velocities.

The results for the highest Froude number $Fn = 0.4$, corresponding to an exceptionally high velocity of 37 kn at full scale, are shown in Figure 13. The simulations results for the heave motion, except for PDr, are close to the experimental results. The pitch motion, however is strictly overpredicted by PD and underpredicted by PDr. Simulations with *panFDS* lead to low pitch motion amplitudes in long waves, but an acceptable agreement in the resonance range. In comparison with results by Riesner [28], the underprediction of the pitch motion is shifted to a higher forward speed and the application of non-inertial motion integration and the restoring coefficient seems to be beneficial for moderate to high forward speeds.

In Figure 14-16 the added resistance of the KCS is plotted over the encounter frequency. The experimental results by Simonsen [33] are denoted by EFD. The accuracy of the measurements peak for $Fn = 0.33$ is questionable and is not further investigated. The calculations and experimental values show a peak of the added resistance coefficient at 4.5-5 $\frac{\text{rad}}{\text{s}}$. The *PDStrip* calculations lead to a higher added resistance than *panFDS* and the experimental results for $Fn = 0.26$ and $Fn = 0.33$. The accuracy at $Fn = 0.4$ is limited due to the overestimated pitch motion, which has significant effect on the added resistance. *panFDS* coefficient calculations differ slightly from experimental results, the calculation with a restoring coefficient is marginally closer to the experiments.

5. Conclusions

In the present paper, different approaches to calculate the hydrodynamic forces by using the impulse response method are presented and compared. The calculations have been conducted with hydrodynamic coefficients obtained from the strip theory code *PDStrip* and the three dimensional rankine source code *panFDS*. The motion behaviours of the Duisburg test case container ship and the Kriso container ship were simulated and the computational results are compared with experimental and computational results.

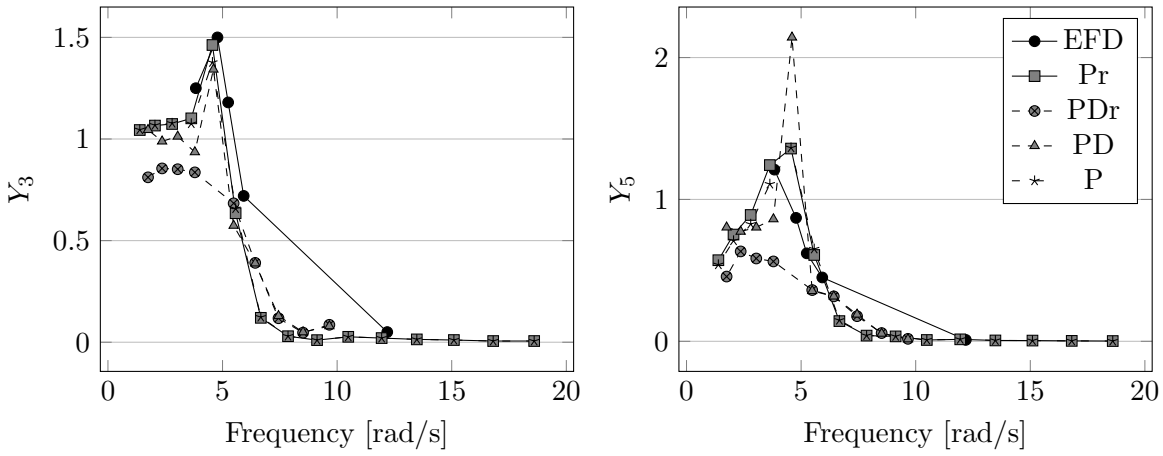

Figure 13: KCS heave (left) and pitch (right) transfer function for $Fn = 0.4$ in head waves

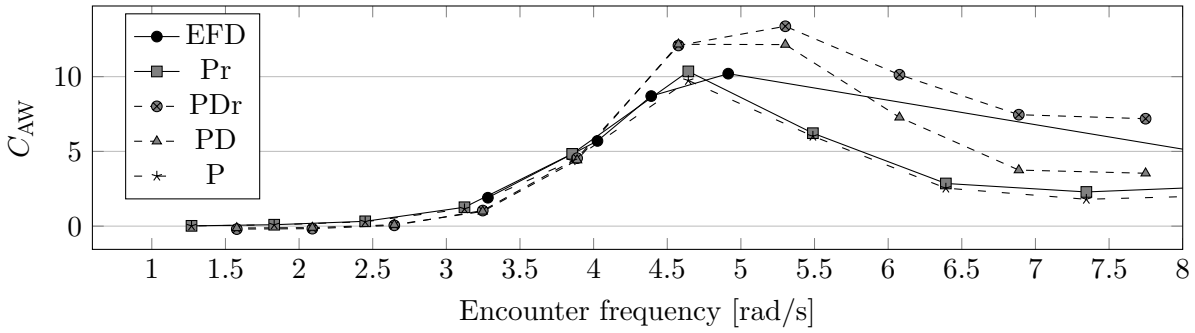

Figure 14: KCS added wave resistance for $Fn = 0.26$ in head waves

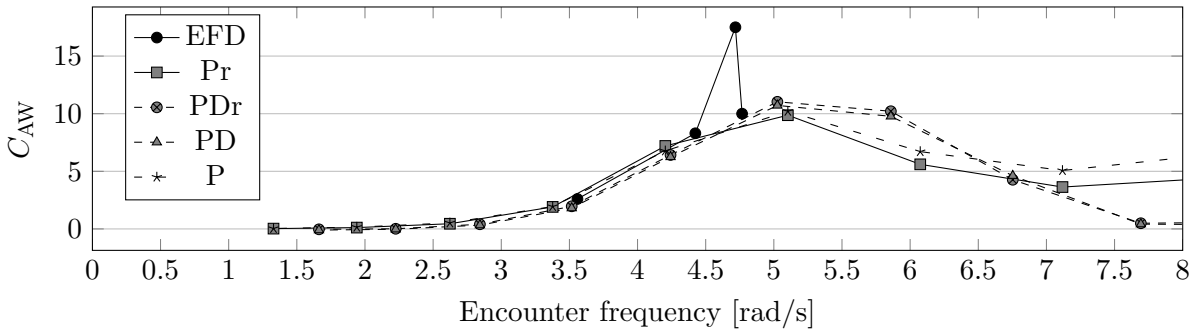

Figure 15: KCS added wave resistance for $Fn = 0.33$ in head waves

Results showed that the diffraction force calculated using a linear coefficient is closer to force amplitudes obtained by RANS simulations than the calculation based on a convolution integral. An exact integration procedure for Froude-Krylov pressures is developed, however numerical accuracy and the simplified determination of the center of pressure limits the accuracy. The application of exact pressure integration should be advantageous in case that the panel dimensions can be adapted to the surface curvature. The current grid generation procedure limits the accuracy, since it is refined uniformly along the ship's body and reduces the shape precision if less panels are used. Another finding is that, the consideration of stationary wave system is beneficial for the derivation of the frequency domain coefficients. This is demonstrated by the fact, that all transfer functions and added resistance curves

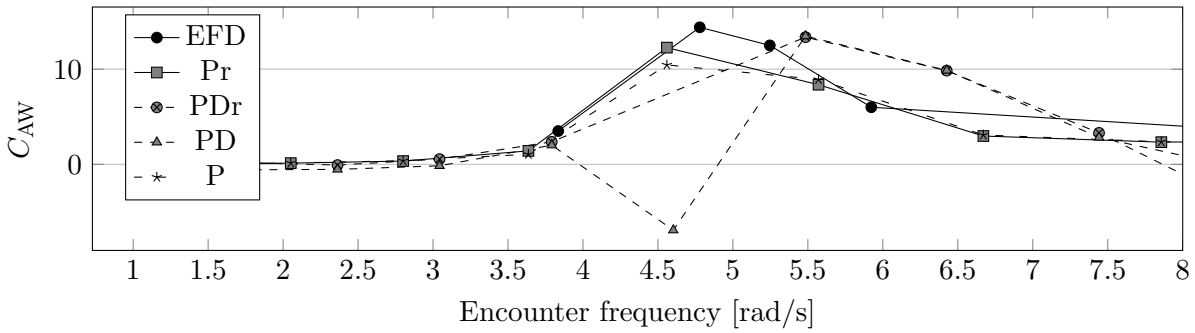

Figure 16: KCS added wave resistance for $Fn = 0.4$ in head waves

with *panFDS* coefficients are closer to experimental results. However, the integration of stationary flow panel pressures in the panel calculations has an negligible effect on heave and pitch forces and motions. The accuracy of the transfer functions with *PDStrip* coefficients is better at lower forward speeds, the applied radiation restoring coefficients increase the accuracy of the calculation for both coefficient sets. The pitch motion at high forward speeds is too small, a limit is identified around $Fn = 0.3$ where the dynamic effects of the flow have a stronger influence on the motion. The added resistance in waves is characterised by the mean value of the additional force in longitudinal direction. It is calculated with high confidence with *panFDS* coefficients, most important finding during the investigation was that the longitudinal center of gravity should be adapted to ensure the desired floating condition.

Future work will focus on implementing the point of pressure integration into the exact Froude-Krylov calculation. Furthermore, an elastic beam theory will be implemented to further investigate whether non linear force calculations are beneficial and if the level of non-linearity of the presented impulse response method can be further increased.

References

[1] K. R. Babu, S. V. K. R. Nelli, A. Bhattacharyya, and R. Datta. Experimental and numerical investigation of green water occurrence for KRISO container ship. *Journal of Ship Research*, 66(01):54–72, dec 2020.

[2] P. Bailey, D. Hudson, W. Price, and P. Temarel. Time simulation of manoeuvring and seakeeping assessments using a unified mathematical model. *Royal Institution of Naval Architects Transactions 2002 Part B*, 144:57–78, 01 2002.

[3] E. J. Ballard, D. A. Hudson, W. G. Price, and P. Temarel. Time domain simulation of symmetric ship motions in waves. *The International Journal of Maritime Engineering*, 145(a2):1, 2003.

[4] V. Bertram, B. Veelo, H. Söding, and K. Graf. Development of a freely available strip method for seakeeping. *Proc. 5th International Conference on Computer and IT Applications in the Maritime Industries*, 01 2006.

[5] W. Cummins. The impulse response function and ship motions. Technical report, David Taylor Model Basin Washington DC, 1962.

[6] O. Detlefsen, L. Theilen, and M. Abdel-Maksoud. Time domain simulation of dynamic positioning manoeuvres based on impulse response functions. In *6th International Conference on Computational Methods in Marine Engineering, MARINE 2015*, page 761, 2015.

[7] S. X. Du, D. A. Hudson, W. G. Price, and P. Temarel. Implicit expressions of static and incident wave pressures over the instantaneous wetted surface of ships. *Proceedings of the Institution of Mechanical Engineers, Part M: Journal of Engineering for the Maritime Environment*, 223(3):239–256, jun 2009.

[8] B. O. el Moctar, T. E. Schellin, and H. Söding. *Numerical Methods for Seakeeping Problems*. Springer International Publishing, 2021.

[9] O. el Moctar, V. Shigunov, and T. Zorn. Duisburg test case: Post-panamax container ship for benchmarking. *Ship Technology Research*, 59(3):50–64, aug 2012.

[10] N. Fonseca and C. G. Soares. Time-domain analysis of large-amplitude vertical ship motions and wave loads. *Journal of Ship Research*, 42(02):139–153, jun 1998.

[11] T. I. Fossen. A nonlinear unified state-space model for ship maneuvering and control in a seaway. *International Journal of Bifurcation and Chaos*, 15(09):2717–2746, sep 2005.

[12] H. Hatecke. The impulse response fitting and ship motions. *Ship Technology Research*, 62(2):97–106, jun 2015.

[13] S. Hirdaris, W. Bai, D. Dessi, A. Ergin, X. Gue, O. Hermundstad, R. Huijsmans, K. Iijima, U. Nielsen, J. Parunov, N. Fonseca, A. Papanikolaou, K. Argyriadis, and A. Incecik. Loads for use in the design of ships and offshore structures. *Ocean Engineering*, 78:131–174, 03 2014.
[14] S. Hirdaris, Y. Lee, G. Mortola, A. Incecik, O. Turan, S. Hong, B. Kim, K. Kim, S. Bennett, S. Miao, and P. Temarel. The influence of nonlinearities on the symmetric hydrodynamic response of a 10,000 TEU container ship. *Ocean Engineering*, 111:166–178, jan 2016.
[15] J. Jiao, Z. Chen, C. Chen, and H. Ren. Time-domain hydroelastic analysis of nonlinear motions and loads on a large bow-flare ship advancing in high irregular seas. *Journal of Marine Science and Technology*, 25(2):426–454, may 2019.
[16] W. Kim, S. Van, and D. Kim. Measurement of flows around modern commercial ship models. *Experiments in fluids*, 31(5):567–578, 2001.
[17] E. Kristiansen, Å. Hjulstad, and O. Egeland. State-space representation of radiation forces in time-domain vessel models. *Ocean Engineering*, 32(17-18):2195–2216, dec 2005.
[18] S. Liu and A. Papanikolaou. Prediction of parametric rolling of ships in single frequency regular and triple frequency group waves. *Ocean Engineering*, 120:274–280, jul 2016.
[19] S. Ma, R. Wang, J. Zhang, W. Y. Duan, R. C. Ertekin, and X. B. Chen. Consistent formulation of ship motions in time-domain simulations by use of the results of the strip theory. *Ship Technology Research*, 63(3):146–158, sep 2016.
[20] T. Perez and T. Fossen. A derivation of high-frequency asymptotic values of 3d added mass and damping based on properties of the cummins equation. *J. Marit. Res*, 5:65–78, 2008.
[21] T. Perez and T. I. Fossen. Kinematic models for manoeuvring and seakeeping of marine vessels. *Modeling, Identification and Control: A Norwegian Research Bulletin*, 28(1):19–30, 2007.
[22] T. Perez and T. I. Fossen. Time- vs. frequency-domain identification of parametric radiation force models for marine structures at zero speed. *Modeling, Identification and Control: A Norwegian Research Bulletin*, 29(1):1–19, 2008.
[23] Y. Peña-Sanchez, N. Faedo, and J. V. Ringwood. A Critical Comparison Between Parametric Approximation Methods for Radiation Forces in Wave Energy Systems. volume All Days of *International Ocean and Polar Engineering Conference*, 06 2019. ISOPE-I-19-521.
[24] S. Rajendran, N. Fonseca, and C. G. Soares. Simplified body nonlinear time domain calculation of vertical ship motions and wave loads in large amplitude waves. *Ocean Engineering*, 107:157–177, oct 2015.
[25] M. Riesner. *Numerical Method to Compute the Wave-Induced Rigid Body and Elastic Response of Ships at Forward Speed*. PhD thesis, University Duisburg-Essen, 2022.
[26] M. Riesner and O. el Moctar. A time domain boundary element method for wave added resistance of ships taking into account viscous effects. *Ocean Engineering*, 162:290–303, aug 2018.
[27] M. Riesner and O. el Moctar. A numerical method to compute global resonant vibrations of ships at forward speed in oblique waves. *Applied Ocean Research*, 108:102520, mar 2021.
[28] M. Riesner, A. von Graefe, V. Shigunov, and O. el Moctar. Prediction of non-linear ship responses in waves considering forward speed effects. *Ship Technology Research*, 63(3):135–145, aug 2016.
[29] J. Rodrigues and C. G. Soares. Froude-krylov forces from exact pressure integrations on adaptive panel meshes in a time domain partially nonlinear model for ship motions. *Ocean Engineering*, 139:169–183, jul 2017.
[30] A. Roessling and J. Ringwood. Finite order approximations to radiation forces for wave energy applications. *Renewable energies offshore*, 359:359–366, 2015.
[31] N. Salvesen, E. Tuck, and O. Faltinsen. Ship motions and sea loads. 1970.
[32] S. Sigmund and O. el Moctar. Numerical and experimental investigation of added resistance of different ship types in short and long waves. *Ocean Engineering*, 147:51–67, jan 2018.
[33] C. D. Simonsen, J. F. Otzen, S. Joncquez, and F. Stern. EFD and CFD for KCS heaving and pitching in regular head waves. *Journal of Marine Science and Technology*, 18(4):435–459, apr 2013.
[34] H. Söding, A. von Graefe, O. el Moctar, and V. Shigunov. Rankine source method for seakeeping predictions. In *Volume 4: Offshore Geotechnics Ronald W. Yeung Honoring Symposium on Offshore and Ship Hydrodynamics*. American Society of Mechanical Engineers, jul 2012.
[35] J. T. Tuitman and Š. Malenica. Fully coupled seakeeping, slamming, and whipping calculations. *Proceedings of the Institution of Mechanical Engineers, Part M: Journal of Engineering for the Maritime Environment*, 223(3):439–456, jun 2009.
[36] J. Wheeler. Method for calculating forces produced by irregular waves. *Journal of Petroleum Technology*, 22(03):359–367, mar 1970.
[37] P. Zhang, T. Zhang, and X. Wang. Hydrodynamic analysis and motions of ship with forward speed via a three-dimensional time-domain panel method. *Journal of Marine Science and Engineering*, 9(1):87, jan 2021.

Appendix A

The derivation of the integration is based on two angles α and β. α describes the angle between the panel longitudinal axis and the transversal axis if seen from above the water surface. It describes, how the y-coordinates at a height z depend on the x-coordinates

$$y(x,z) = y_\mathrm{s}(z) + (x(z) - x_\mathrm{s}(z)) \cdot \tan(\alpha)\,, \tag{42}$$

$$\alpha = \begin{cases} \arctan(n_\mathrm{x}/n_\mathrm{y}) & n_\mathrm{y} \neq 0 \\ \frac{\pi}{2} & n_\mathrm{y} = 0 \end{cases}. \tag{43}$$

The coordinates y_s and x_s describe an outer edge of the panel and the indices x, y of n the entries of the normal vector in the respective directions.
β describes the orientation of the angle between the vertical coordinate axis z and the panel

$$\beta = \arccos(n_\mathrm{z})\,. \tag{44}$$

The triangle is described by three corner points $\vec{x}_0$-$\vec{x}_2$, which are sorted by their z-coordinate. The functions for the x-coordinates of the outer edges are

$$x_{s,1}(z) = x_0 + \frac{z - z_0}{z_1 - z_0} \cdot (x_1 - x_0)\,, \tag{45}$$

$$x_{e,1}(z) = x_0 + \frac{z - z_0}{z_2 - z_0} \cdot (x_2 - x_0)\,, \tag{46}$$

$$x_{s,2}(z) = x_2 + \frac{z - z_2}{z_0 - z_2} \cdot (x_0 - x_2)\,, \tag{47}$$

$$x_{e,2}(z) = x_2 + \frac{z - z_2}{z_1 - z_2} \cdot (x_1 - x_2)\,. \tag{48}$$

At a constant value of z, the Froude-Krylov pressure can be integrated along the breadth $B(z)$ of the panel

$$B(z) = \tfrac{x_\mathrm{e} - x_\mathrm{s}}{\cos\alpha}\,. \tag{49}$$

With the force per height defined as the integral of the instationary Bernoulli pressure

$$f(z) = -\rho\hat{\zeta}ge^{-k(z-\zeta)} \int_0^B \cos(\omega t - kx\cos\mu + ky\sin\mu + \varphi)\,\mathrm{d}B\,. \tag{50}$$

If one inserts the relationships from (43) and (49), the resulting force per length is equal to

$$f(z) = \frac{\rho\hat{\zeta}ge^{-k(z-\zeta)}}{k\cos(\alpha+\mu)} \Big[\sin(\omega t - k\frac{x_e - x_s}{\cos\alpha}\cos(\alpha+\mu) - kx_s\cos\mu + ky_s\sin\mu + \varphi) \tag{51}$$

$$- \sin(\omega t - kx_s\cos\mu + ky_s\sin\mu + \varphi)\Big] \tag{52}$$

The integration along the z-direction is done by describing the height L of the two separate areas with the angle β

$$L_1 = \frac{z_1 - z_0}{\sin\beta}\,, \tag{53}$$

$$L_2 = \frac{z_1 - z_2}{\sin\beta}\,. \tag{54}$$

$$F_{fk,1} = a_1 \int_0^{L_{z,1}} e^{-k(L_z\sin\beta + z_0)}(\sin(b_1 + b_2 L_z) - \sin(c_1 + c_2 L_z)) \tag{55}$$

The resulting formulae are shown in subsection 2.4.
The following abbreviations are used:

$$a_1 = \frac{\rho g \hat{\zeta} e^{k\zeta} e^{-kz_0}}{k\cos(\alpha+\mu)} \qquad a_2 = \frac{\rho g \hat{\zeta} e^{k\zeta} e^{-kz_2}}{k\cos(\alpha+\mu)} \qquad a_3 = \frac{\rho g \zeta e^{-k(z_0-\zeta)}}{k\cos\mu}$$

$$b_1 = c_1 = \omega t + \varphi - k(x_0\cos\mu - y_0\sin\mu)$$

$$b_2 = k\sin\beta\left(-\frac{\cos(\alpha+\mu)}{\cos\alpha}\left(\frac{x_2-x_0}{z_2-z_0}-\frac{x_1-x_0}{z_1-z_0}\right)-\cos\mu\frac{x_1-x_0}{z_1-z_0}+\sin\mu\frac{y_1-y_0}{z_1-z_0}\right)$$

$$b_3 = c_3 = \omega t + \varphi - k(x_2\cos\mu - y_2\sin\mu)$$

$$b_4 = k\sin\beta\left(-\frac{\cos(\mu+\alpha)}{\cos\alpha}\left(\frac{x_2-x_0}{z_2-z_0}-\frac{x_2-x_1}{z_2-z_1}\right)-\cos\mu\frac{x_2-x_1}{z_2-z_1}+\sin\mu\frac{y_2-y_1}{z_2-z_1}\right)$$

$$b_5 = \begin{cases} \omega t + \varphi - kx_0\cos\mu + k\frac{x_2-x_0}{y_2-y_0}y_0\cos\mu & y_2-y_0 \neq 0 \\ 0 & y_2-y_0 = 0 \end{cases}$$

$$b_6 = \omega t + \varphi - kx_0\cos\mu + k\frac{x_1-x_0}{y_1-y_0}y_0\cos\mu$$

$$b_7 = \begin{cases} -k\frac{x_2-x_0}{y_2-y_0}\cos\mu - k\sin\mu & y_2-y_0 \neq 0 \\ 0 & y_2-y_0 = 0 \end{cases}$$

$$b_8 = \omega t + \varphi - kx_1\cos\mu + k\frac{x_2-x_1}{y_2-y_1}y_1\cos\mu$$

$$c_2 = k\sin\beta\left(-\frac{x_1-x_0}{z_1-z_0}\cos\mu+\frac{y_1-y_0}{z_1-z_0}\sin\mu\right)$$

$$c_4 = k\sin\beta(-\cos\mu\frac{x_2-x_1}{z_2-z_1}+\sin\mu\frac{y_2-y_1}{z_2-z_1})$$

$$c_5 = \begin{cases} -k\frac{x_2-x_0}{y_2-y_0}\cos\mu - k\sin\mu & y_2-y_0 \neq 0 \\ 0 & y_2-y_0 = 0 \end{cases}$$

$$c_6 = -k\frac{x_1-x_0}{y_1-y_0}\cos\mu - k\sin\mu$$

$$c_7 = \begin{cases} -k\frac{x_2-x_0}{y_2-y_0}\cos\mu - k\sin\mu & y_2-y_0 \neq 0 \\ 0 & y_2-y_0 = 0 \end{cases}$$

$$c_8 = -k\frac{x_2-x_1}{y_2-y_1}\cos\mu - k\sin\mu$$

$$f_{fk,11} = \begin{cases} \frac{\cos(b_6+c_6y_1)-\cos(b_6+c_6y_0)}{c_6} & c_6 \neq 0 \\ -\sin(b_6)\cdot(y_1-y_0) & c_6 = 0 \end{cases} \qquad f_{fk,12} = \begin{cases} -\frac{\cos(b_5+c_5y_1)-\cos(b_5+c_5y_0)}{c_5} & c_5 \neq 0 \\ \sin(b_5)\cdot(y_1-y_0) & c_5 = 0 \end{cases}$$

$$f_{fk,21} = \begin{cases} \frac{\cos(b_8+c_8y_2)-\cos(b_8+c_8y_1)}{c_8} & c_8 \neq 0 \\ -\sin(b_8)(y_2-y_1) & c_8 = 0 \end{cases} \qquad f_{fk,22} = \begin{cases} -\frac{\cos(b_7+c_7y_2)-\cos(b_7+c_7y_1)}{c_7} & c_7 \neq 0 \\ \sin(b_7)(y_2-y_1) & c_7 = 0 \end{cases}$$